Available online at www.sciencedirect.com
ScienceDirect
Environmental Modelling & Software 22 (2007) 488–501
Environmental Modelling & Software
www.elsevier.com/locate/envsoft

Simulation of constituent transport using a reduced 3D constituent transport model (CTM) driven by HF Radar: Model application and error analysis

Temitope O. Ojo*, James S. Bonner, Cheryl A. Page

Civil Engineering Department, Texas A&M University, College Station, TX 77843-3136, USA

Received 11 November 2004; received in revised form 5 July 2005; accepted 12 February 2006
Available online 26 May 2006

Abstract

Data-driven constituent transport models (CTM), which take surface current measurements from High Frequency (HF) Radar as input can be applied within the context of real-time environmental monitoring, oceanographic assessment, response to episodic events, as well as search and rescue in surface waters.This paper discusses a numerical method that allows for the evaluation of diffusion coefficients in anisotropic flow fields from surface current measurements using HF Radar. The numerical scheme developed was incorporated into a data-driven CTM and through model error analyses, the effects of using spatially variable transport coefficients on model predictions were examined. The error analyses were performed on the model by varying the cell Reynolds number, $Re = f(\boldsymbol{u},\boldsymbol{K},\Delta\boldsymbol{x})$ between 0.15 and 100, where $\boldsymbol{u}$ is the velocity vector within the flow field, $\boldsymbol{K}$ is a diffusivity tensor and $\Delta\boldsymbol{x}$ is the computational grid cell size.Two instantaneous releases of conservative material were then modeled, the model being initialized at two different locations within the domain. From the two simulation runs, marked differences in the predicted spatial extent of the conservative material resulting from the spatially varying diffusivity values within the study area were observed. Model predictions in terms of variance or size estimates of a diffusing patch were found to be more affected from using inaccurate diffusivity estimates, and less affected from using inaccurate current measurements. The largest errors occurred at $Re > 2$ associated with changing diffusivity values, going up to as much as a 25-fold difference in variance estimates at $Re = 100$. Very little effect on variance estimates due to varying velocity values were observed even at $Re > 2$. This model was applied within the framework of constituent tracking to Corpus Christi Bay in the Texas Gulf of Mexico region.

Keywords: Coastal; Diffusion coefficients; Mixing processes; Modeling; Pollutant transport; Transport processes; USA; Gulf of Mexico; Texas; Corpus Christi Bay

1. Introduction

Mixing processes (turbulence and shear) in surface waters are important as they govern the overall distribution of constituents within the domain of interest, including constituents that may be biogenic or anthropogenic in origin. In conjunction with sampling and measurements, constituent transport modeling (CTM) can be a valuable tool for environmental assessments, forming the bedrock of most water quality and pollutant tracking applications in surface waters. A number of these models have been developed for use in various applications covering a wide range of spatial and temporal scales. An excellent review of models and their applications can be found in Martin and McCutcheon (1998) while Reed et al. (2004) describes an application for simulating dispersant application in a shallow bay. Mechanistic models such as ADIOS developed by the National Oceanic and Atmospheric Administration Hazardous Materials Response Division (Lehr et al., 2002) and SIMAP developed by Applied Science Associates (McCay, 2003) have specific application to oil spills while others such as WQMAP (Spaulding et al., 1999) are more general in their application to water quality. These models are based on the solution of

* Corresponding author. Tel.: +1 979 458 3878.
E-mail address: tojo@serf.tamus.edu (T.O. Ojo).

1364-8152/$ - see front matter © 2006 Elsevier Ltd. All rights reserved.
doi:10.1016/j.envsoft.2006.02.010

coupled sets of partial differential equations (PDEs) comprising two distinct modules. One module provides hydrodynamic information through direct numerical simulation (DNS) while the other module provides solution from the constituent (mass, heat, solute, etc.) transport equations. The DNS module is a set of PDEs, comprising the well-known Navier–Stokes equations based on momentum conservation while the constituent transport module is a set of advection–diffusion reaction PDEs based on mass conservation laws.

The governing equation of constituent transport will have a diffusive component that is based on Fick's law of diffusion and applicable when the scale of the transport phenomenon is larger than the characteristic scale (time or length) of the diffusion process. This derives from the material balance in turbulent flow within an elemental fluid volume accounting for the combined turbulent fluctuations in the currents field and the constituent of interest. For conservative materials, the resultant temporal gradient (or time rate of change) of solute concentration is the sum of the spatial gradients of the advective and diffusive fluxes. This argument although developed within the context of turbulence can be extended to include other effects that are known to influence diffusive processes such as current shear (Bowden and Howe, 1963; Elliot, 1986). Since the turbulent field in bays exhibits anisotropy, one would expect to find the diffusive process characterized by the diffusivity values exhibiting spatial–temporal variability (Ojo and Bonner, 2002). The spatial variability of diffusivity was investigated as part of this study.

From the foregoing, two sets of coefficients are required in the governing equation of transport: the advection (velocity) coefficients and the diffusion coefficients (turbulence or shear). Advection coefficients are provided either through direct observations or through DNS as outlined above and in this study, these were obtained from direct observations using HF Radar. Diffusion coefficients can be estimated using one of the following methods:

- Method A: From the evaluation of the temporal variation of the magnitude and direction of currents (Paul et al., 1989; Taylor, 1920, 1954).
- Method B: Based on the evaluation of the spatial variation of the velocity field (Csanady, 1980 (reprinted); Elder, 1958; Taylor, 1953).
- Method C: From the evaluation of the first and second moments of concentration distribution of a diffusing cloud (Murthy, 1975; Okubo, 1971).
- Method D: An inverse problem based on the governing equation of advection–diffusion (Ernest et al., 1991; Lam et al., 1983).

The first three of these four methods have been applied in a series of related studies within Corpus Christi Bay (Ojo et al., submitted for publication-a-b, in press) aimed at estimating diffusivity values from direct observations of current in surface waters.

The spatial extent typical of bays and estuaries is such that the incorporation of hydrodynamic information into a CTM defaults to the DNS method, which couples a hydrodynamic numerical scheme to a mass transport scheme within the modeling framework. While the required model parameterization are in many cases based on turbulence–closure schemes that have been developed by a number of researchers (Wijesekera et al., 2003), there are inherent uncertainties in their application especially within shallow wind-driven bodies of water typical of Texas bays. Improved accuracy can be achieved in CTM applications by incorporating direct measurements of velocity (or advective coefficients) in near real-time into constituent transport and water quality models predicated on recent advances in surface current measurements using HF Radar.

As outlined above, the diffusion coefficients can be estimated from the velocity time series, which are then incorporated into the modeling framework. In this study, Method A was applied where the diffusion coefficients were evaluated using the statistical properties of a turbulent flow field, leading to the development of a data-driven CTM. Since HF Radar only provides surface currents (2D velocity profile) within the domain of interest, in order to develop a 3D current field, Acoustic Doppler Current Profiler (ADCP) measurements were used in providing velocity time series along the vertical coordinate axis.

The objectives of this study are the following:

1. To estimate diffusion coefficients based on direct observations of hydrodynamic data on spatial scales $\sim$30 km and temporal scales covering several tidal cycles.
2. To develop a framework for incorporating direct hydrodynamic observations and derived turbulent diffusivities into a simplified data-driven CTM.
3. To examine through model error analysis:
   a. The effect of inaccuracies associated with current measurements on model predictions.
   b. The results of using spatially averaged values of diffusion coefficients typically obtained from diffusion diagrams or tracer experiments vs. using spatially distributed values obtained through current measurements as outlined above.
4. To apply the resulting simplified data-driven CTM to near real-time constituent tracking in Corpus Christi Bay, Texas.

The integration of numerical modeling (Ernest et al., 1991; Lee et al., 2000; Sterling et al., 2004a,b) with real-time measurements (Ojo et al., 2003) is important for characterizing bays and estuaries as well as within the context of response to episodic events in surface waters. This is part of ongoing research within our laboratory with the overarching objective of developing an operational environmental and oceanographic assessment system for the coastal and nearshore environments.

2. Background theory

The generalized form of the governing equations that form a coupled set for a CTM is given in Eqs. (1) and (2) where u_x, u_y, u_z are the component velocities, N_x, N_y, N_z are eddy

viscosities, K_x, K_y, K_z are diffusivities along each of the coordinate axis, g is the gravitational constant, ρ is the fluid density, R_i represents a source/sink term and C_i the concentration of the i-th constituent. Numerical solutions to these equations can be obtained using any one of a variety of computational techniques (Fletcher, 1991). A simplified set of these equations obtained by uncoupling the momentum Eq. (1) will result in Eq. (2) where the subscript i denotes the i-th constituent of interest.

$$\left.\begin{aligned}
&\text{Continuity}: \frac{\partial u_x}{\partial x}+\frac{\partial u_y}{\partial y}+\frac{\partial u_z}{\partial z}=q\\
&\text{Momentum } x \text{ Direction}: \frac{\partial u_x}{\partial t}=-\frac{\partial(u_x u_x)}{\partial x}-\frac{\partial(u_y u_x)}{\partial y}-\frac{\partial(u_z u_x)}{\partial z}+\frac{\partial}{\partial x}\left[\left(\nu+\frac{N_x}{\rho}\right)\frac{\partial u_x}{\partial x}\right]+\frac{\partial}{\partial y}\left[\left(\nu+\frac{N_y}{\rho}\right)\frac{\partial u_x}{\partial y}\right]+\frac{\partial}{\partial z}\left[\left(\nu+\frac{N_z}{\rho}\right)\frac{\partial u_x}{\partial z}\right]+g_x\\
&\text{Momentum } y \text{ Direction}: \frac{\partial u_y}{\partial t}=-\frac{\partial(u_x u_y)}{\partial x}-\frac{\partial(u_y u_y)}{\partial y}-\frac{\partial(u_z u_y)}{\partial z}+\frac{\partial}{\partial x}\left[\left(\nu+\frac{N_x}{\rho}\right)\frac{\partial u_y}{\partial x}\right]+\frac{\partial}{\partial y}\left[\left(\nu+\frac{N_y}{\rho}\right)\frac{\partial u_y}{\partial y}\right]+\frac{\partial}{\partial z}\left[\left(\nu+\frac{N_z}{\rho}\right)\frac{\partial u_y}{\partial z}\right]+g_y\\
&\text{Momentum } z \text{ Direction}: \frac{\partial u_z}{\partial t}=-\frac{\partial(u_x u_z)}{\partial x}-\frac{\partial(u_y u_z)}{\partial y}-\frac{\partial(u_z u_z)}{\partial z}+\frac{\partial}{\partial x}\left[\left(\nu+\frac{N_x}{\rho}\right)\frac{\partial u_z}{\partial x}\right]+\frac{\partial}{\partial y}\left[\left(\nu+\frac{N_y}{\rho}\right)\frac{\partial u_z}{\partial y}\right]+\frac{\partial}{\partial z}\left[\left(\nu+\frac{N_z}{\rho}\right)\frac{\partial u_z}{\partial z}\right]+g_z
\end{aligned}\right\}\text{Hydrodynamic Model} \tag{1}$$

In the application of Eq. (2) for the implementation of a simplified CTM, two sets of coefficients are required. The first set relating to the advective flux is obtained by direct observation, and the other set relating to the diffusive flux is obtained through the autocorrelation functions (ACF) of the respective velocity time series. Velocity components u_x, u_y along the x- (east–west) and y- (north–south) coordinate directions, respectively, data are obtained from HF Radar and the vertical component, u_z along the z-coordinate direction obtained from ADCP measurements for a 3D model implementation.

$$\left.\begin{aligned}
\text{Constituent Transport}: \frac{\partial C_i}{\partial t}=&-\frac{\partial(uC_i)}{\partial x}-\frac{\partial(vC_i)}{\partial y}-\frac{\partial(wC_i)}{\partial z}\\
&+\frac{\partial}{\partial x}\left[K_x\frac{\partial C_i}{\partial x}\right]+\frac{\partial}{\partial y}\left[K_y\frac{\partial C_i}{\partial y}\right]\\
&+\frac{\partial}{\partial z}\left[K_z\frac{\partial C_i}{\partial z}\right]\\
&\pm R(C_i)
\end{aligned}\right\}\text{Transport} \tag{2}$$

$$(\text{rate} = \text{advective flux} + \text{diffusive flux} \pm \text{source/sink})$$

2.1. Diffusion coefficients for simplified CTM

It has been shown by Batchelor (1953) that turbulent diffusion in a flow field is related to the autocorrelation function (ACF), R_i of the velocity time series $u(x,y,z,t)$. Following the work of Taylor (Taylor, 1920, 1953), these coefficients are defined as follows:

$$K_i = \overline{u}_i^2 T_i, \quad T_i = \int_0^t R_i(\tau)\mathrm{d}\tau, \quad R_i(\tau) = \frac{\overline{u_i'(t)u_i'(t+\tau)}}{\overline{u_i'(t)}^2} \tag{3}$$

$$0 < R < 1 \quad \text{for } 0 < \tau < \infty$$

For a fluid in a turbulent flow, the turbulent velocity field is represented by the time series $u_i(t) = \overline{u_i(t)} + u_i'(t)$ and R_i is the autocorrelation function of the velocity time series, the overbar indicating averaged values over the ensemble of samples and T_i is the characteristic time scale of the process. While several analytical models have been put forward from statistical hydromechanics (e.g. Gaussian, Markov, etc.), it is possible to obtain numerical estimates for R_i and the numerical method was used in this study. The values for R_i were obtained directly from the discretized current measurements following which a numerical integration on R_i was performed to obtain the diffusion coefficient K_i. The algorithmic aspects of the above scheme were implemented in MATLAB™, a high-level engineering and scientific programming language.

2.2. Model error analysis

Two sources of error are identified in the implementation of a typical CTM. Discretization errors or truncation errors are associated with numerical approximations of the differencing. The other source of errors is inherent in the application of model coefficients. Two forms of truncation error typically introduced through the discretization are termed as numerical dissipation (artificial diffusion) and numerical dispersion. The former manifests as a spatial lead or lag while the latter produces a reduction in the concentration levels relative to the analytical results. Both are dependent on the even and odd higher-order spatial derivative approximations, respectively, and varies with the cell Reynolds number, $Re = u_i\Delta x/K_i$ $(i = x,\ y,\ z)$ where K_i represents the respective diffusivities and u_i the respective velocities along the coordinate axes.

The truncation errors can be quantified by comparing model results with the closed-form, which for a pulse discharge of mass M_0, is given by Eq. (4) below.

$$c^*(x,y,z,t) = \frac{M_0}{8(\pi)^{3/2}\left(K_xK_yK_z\right)^{1/2}t^{3/2}}\exp\left[-\frac{1}{4}\left\{\frac{(x-u_xt)^2}{K_xt} + \frac{(y-u_yt)^2}{K_yt} + \frac{(z-u_zt)^2}{K_zt}\right\}\right] \tag{4}$$

A forward time, centered space (FTCS) finite difference approximation on a spatial $[i \times j \times k]$ – temporal $[\times n]$ grid for Eq. (2) results in a set of discretized algebraic equations (DAE).

$$\begin{aligned}\frac{\Delta c^{n+1}_{i,j,k}}{\Delta t} = &- u_x\frac{c^n_{i+1,j,k} - c^n_{i-1,j,k}}{2\Delta x} - u_y\frac{c^n_{i,j+1,k} - c^n_{i,j-1,k}}{2\Delta y}\\ &- u_z\frac{c^n_{i,j,k+1} - c^n_{i,j,k-1}}{2\Delta y} + K_x\frac{c^n_{i+1,j,k} - 2c^n_{i,j,k} + c^n_{i-1,j,k}}{\Delta x^2}\\ &+ K_y\frac{c^n_{i,j-1,k} - 2c^n_{i,j,k} + c^n_{i,j+1,k}}{\Delta y^2}\\ &+ K_z\frac{c^n_{i,j,k-1} - 2c^n_{i,j,k} + c^n_{i,j,k+1}}{\Delta z^2}\end{aligned} \tag{5}$$

Eq. (5) can be written in matrix form as follows:

$$\frac{\Delta c^{n+1}_{i,j,k}}{\Delta t} = \left[\frac{-u_x}{2\Delta x}\ \frac{-u_y}{2\Delta y}\ \frac{-u_z}{2\Delta z}\ \frac{K_x}{\Delta x^2}\ \frac{K_y}{\Delta y^2}\ \frac{K_z}{\Delta z^2}\right]\begin{bmatrix} c^n_{i+1,j,k} - c^n_{i-1,j,k}\\ c^n_{i,j+1,k} - c^n_{i,j-1,k}\\ c^n_{i,j,k+1} - c^n_{i,j,k-1}\\ c^n_{i+1,j,k} - 2c^n_{i,j,k} + c^n_{i-1,j,k}\\ c^n_{i,j+1,k} - 2c^n_{i,j,k} + c^n_{i,j-1,k}\\ c^n_{i,j,k+1} - 2c^n_{i,j,k} + c^n_{i,j,k-1}\end{bmatrix} \tag{6}$$

This can be written as a set of ordinary differential equations (ODE) by partial discretization writing the LHS as a total derivative ($dc/dt = r$) in terms of spatial differential approximations on the RHS.

$$\boldsymbol{r} = \boldsymbol{SC} \tag{7}$$

where $\boldsymbol{r}$ is evaluated as the time rate of change of concentration at a node (i, j, k) on the spatial grid having a concentration, $c_{i,j,k}$ at time-step n; $\boldsymbol{S}$ is a matrix of coefficients and $\boldsymbol{C}$, a matrix of concentration differentials evaluated at surrounding node points. This method-of-lines formulation of an unsteady advection–diffusion transport with appropriate boundary conditions (B.C.) and forward-stepping in time has a truncation error of $O(\Delta x^2, \Delta y^2, \Delta z^2)$ the initial and boundary conditions being specified appropriately.

Since Eq. (4) is only valid for constant coefficients, solution of Eq. (7) will be analyzed with constant coefficients for comparison against the closed-form. Although Ruan et al. (1999) proposed a generalized scheme that allows for spatially distributed coefficients to be used in the evaluation of the numerical accuracy, for the purpose of error analysis in this study, the localized values for u_x, u_y, u_z, K_x, K_y, and K_z will be taken as constant. The accuracy check on the discretization can be performed using the spatially aggregated root-mean-square error, RMSE as follows:

$$\mathrm{RMSE} = \frac{\Delta x\Delta y\Delta z}{M_0}\sqrt{\left\{\sum_i^N\left[c_{i,j,k} - c^*(x,y,z)\right]^2\right\}} \tag{8}$$

where N is the number of nodes in the computational grid. The RMSE compares the numerical solution with the analytical. Since the latter has no discretization errors associated with it, the RMSE should therefore give a relative indication of the amount of numerical dispersion and dissipation inherent in the discretization. Having quantified the accuracy of the numerical solution, the overall uncertainties in model predictions associated with the model coefficients resulting from errors associated with inaccuracies in velocity measurements and errors associated with estimation of diffusion coefficients can be established.

3. Methods and materials

This study focuses on intermediate scale mixing processes falling within the temporal scale of 3–10 days or length scale ~10 km. The categorized scale of mixing processes in open waters is as shown in Table 1.

The study area covers a horizontal scale ~25 × 25 km and a vertical scale ~4 m. Two scenarios were modeled comprising of an instantaneous discharge at two different locations. In both scenarios, the model was initialized with the same concentration of material at the same time within the tidal cycle and the diffusing cloud was then "tracked" over the course of several tidal cycles.

3.1. Instrumentation and data analyses

Surface current required as hydrodynamic input into the model was obtained from HF Radar measurements. The Seasonde™ HF Radar equipment manufactured by CODAR Ocean Sensors, which is operated as part of a coastal observatory network maintained by our research group (Kelly et al., 2004) has a range up to 25 km at a grid resolution of 1000 m. Operating on the principle of Bragg Scattering of high frequency (HF) electromagnetic waves incident on surface waves (Barrick et al., 1977), it continuously measures surface currents at 1-h intervals over the entire study area. Spatial interpolation schemes and temporal filtering routines were written and applied for data pre-processing to account for data dropouts and to allow the velocity measurements to be in step with the requirements of the numerical scheme used in evaluation of dispersion coefficients.

3.2. Estimating turbulent diffusivity from current measurements

Turbulent diffusivity defined in terms of the time variation of the velocity autocorrelation function following Taylor's analysis was used by List et al. in a set of experiments to evaluate diffusion coefficients from velocity time series using Langrangian drifters (List et al., 1990). Prior to this Okubo had

Table 1
Categorization of scales of mixing processes in open waters

Small scale	Intermediate scale	Large scale
Temporal scale <24 h, spatial scale between 0 and 10 km	Temporal scale between 1 and 100 days, spatial scale between 10 and 300 km	Temporal sale >100 days, encompassing the ocean basin

developed a set of oceanic diffusion diagrams based on tracer experiments in surface waters and established a 4/3 power-law relation between turbulent diffusion coefficients and a diffusion length scale. O'Connor et al. performed assessments in the 106-mile region, a waste disposal site off the coast of New Jersey basing their analysis on the relationship between spatial variance and variance of the velocity field (O'Connor et al., 1985). The dispersion estimates were obtained from the variance–covariance matrix of the velocity time series through a scaling dependence.

In this study, the approach was to numerically analyze the velocity time series for the evaluation of the time scale of the diffusion process, T_i through the numerically determined autocorrelation function, R_i. Since the scale of the analyses was of the order of several days, the tidal variations in velocity was treated as turbulent fluctuations relative to a mean de-tided velocity, $\overline{u}_i$ ($i = x, y, z$) along the orthogonal coordinate axes. The preprocessed velocity time series was used in conjunction with Eq. (3) to derive the spatially distributed diffusion coefficients. The discretized form of this equation was used in a numerical scheme to derive the diffusion coefficients at each node within the computational domain.

3.3. Modeling framework for data-driven CTM

Since the reduced or simplified model used in this study incorporated direct observations of velocity and diffusion coefficients, the resulting partial differential equation (PDE) was solved in a time-stepping routine using a PDE solver based on the method-of-lines. The velocity coefficients on the surface, which coincides with the top horizontal plane, were provided by radar while sub-surface currents on each of the remaining four horizontal planes were obtained through a linear representation of current profiles from ADCP.

The finite difference 3D computational domain is shown in Fig. 1 and it covers a spatial extent of 25×25 km on a structured base grid with 1000 m resolution in the horizontal and 1 m resolution in the vertical plane. The PDE solver VLUGR-3 (Blom and Verwer, 1996), a three-dimensional vectorizable adaptive grid finite difference scheme accommodates irregular boundaries and the computational grid was made to conform approximately to the outline of the study area. The grid was generated interactively through a graphical interface that allowed for masking of land areas. Five horizontal planes were generated in this implementation having 2030 nodes on the base grid. The solver's adaptive grid scheme allows for on-the-fly grid refinement requiring automatic adjustment to the computational time-step within sections of the computational domain where sharp gradients may result especially at the start of the simulation and at the boundaries.

Output from the model simulation was written to individual ASCII files every hour for the duration of the computer experiment while MATLAB® based data visualization and analyses routines were applied for data post-processing. The modeling framework as described is presented graphically in Fig. 2. Within this framework, algorithms were developed for data pre- and post-processing, numerical computation of diffusivities, grid generation, as well as visualization of model output.

3.4. Model error analysis

The purpose of the error analysis was to verify the effect of inaccuracies in the model predictions resulting from the discretization of the governing equations. For this part of the study, uniform coefficients (velocity and diffusion) were initially used in the model in order to compare the model results against the analytical solution.

It is imperative that the solver should introduce very little artificial diffusion (which may swamp out physical diffusion) and should accurately locate the center of mass of the concentration profile. In this study, the method-of-moments was applied to determine the spatial location and extent of the diffusing cloud and therefore the amount of artificial diffusion and numerical dissipation introduced by the model for various values of *Re*. The first moment of the concentration profile given in Eq. (10) locates the center of mass while the second moment given in Eq. (11) evaluates the variance (a measure of dispersion). These values for the center of mass and variance computed from the numerical scheme were compared with those from the exact solution following which the estimate of the error was determined from using Eq. (8).

$$M_0 = \int_{-\infty}^{\infty}\int\int c(x,y,z,t)\mathrm{d}x\,\mathrm{d}y\,\mathrm{d}z \tag{9}$$

$$x_0 = \frac{1}{M_0}\int_{-\infty}^{\infty}\int\int xc(x,y,z,t)\mathrm{d}x\,\mathrm{d}y\,\mathrm{d}z$$
$$y_0 = \frac{1}{M_0}\int_{-\infty}^{\infty}\int\int yc(x,y,z,t)\mathrm{d}x\,\mathrm{d}y\,\mathrm{d}z \tag{10}$$

$$S_x^2(t) = \frac{1}{M_0}\int_{-\infty}^{\infty}\int\int (x-x_0)^2 c(x,y,z,t)\mathrm{d}x\,\mathrm{d}y\,\mathrm{d}z$$
$$S_y^2(t) = \frac{1}{M_0}\int_{-\infty}^{\infty}\int\int (y-y_0)^2 c(x,y,z,t)\mathrm{d}x\,\mathrm{d}y\,\mathrm{d}z \tag{11}$$

Having established the numerical accuracy of the model, spatially varying coefficients were applied in the advection–diffusion model. The scheme used for generating the diffusion coefficients was described earlier. The computational domain was initially divided into a $26 \times 26 \times 5$ grid and a level-4 grid refinement specified for the solver. Each level of grid refinement results

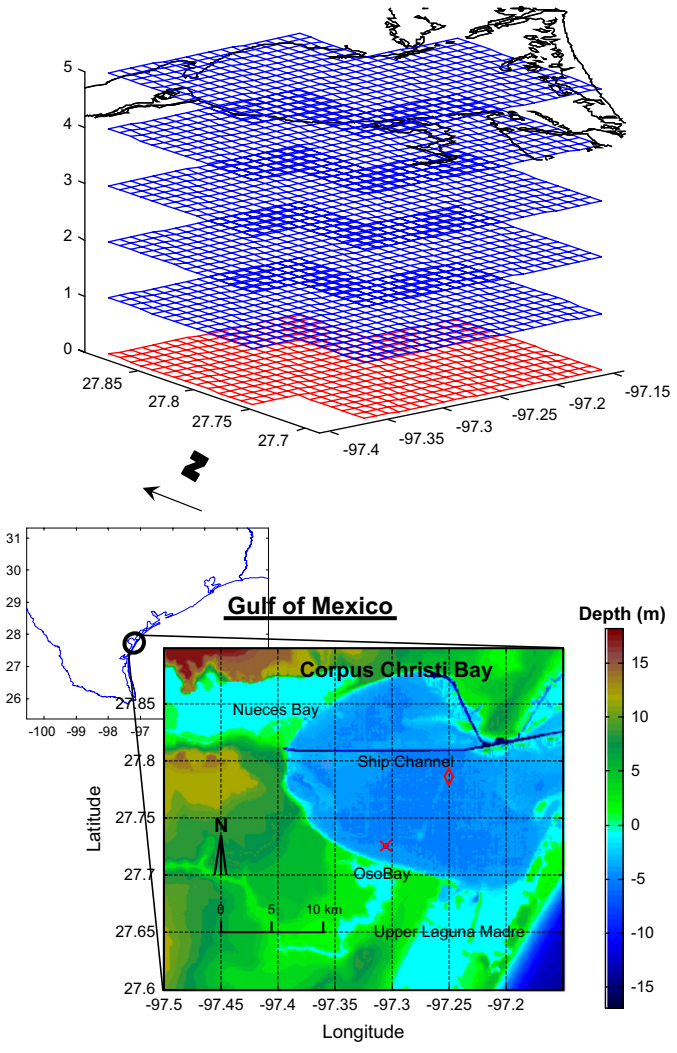

Fig. 1. Top panel; finite difference computational grid. Bottom panel; location and bathymetry of the study area, relatively shallow and flat at ~4 m (× - approximate injection location for model run #1; ◇ - approximate injection location for model run #2).

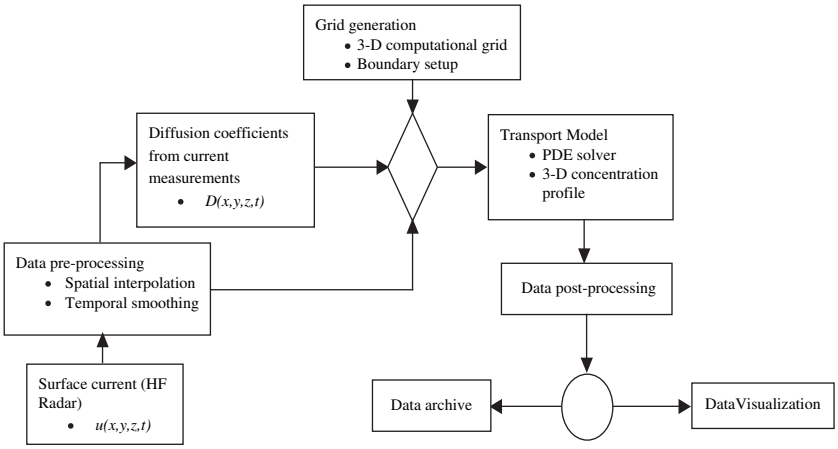

Fig. 2. Framework for data-driven transport model.

in halving of the grid spacing in the areas where sharp gradients were found to occur during computation.

3.5. Model simulation runs

Two scenarios were modeled in this study with the same amount of instantaneous tracer release at two different locations corresponding to regions where significant differences in diffusivity values could be observed. The model grid resolution was set at 1000 m in the horizontal and 1 m in the vertical. Hourly surface current measurements were incorporated directly into the model providing the advective flux coefficients. The same dataset was then used in obtaining the diffusive flux coefficients using the autocorrelation function, R_i of the velocity time series as described in the preceding section. Vertical current profiles were obtained using a boat mounted downward looking ADCP during a series of dye-tracer experiments from which a first-order polynomial was found to provide suitable approximation to the vertical profile of current. The linear velocity profile was applied resulting in a 3D implementation of the computational scheme, this profile being assumed to be invariant over the computational domain.

In each of the simulation runs, initial conditions were established by applying a pulse discharge of material with an initial concentration, $C_o = 0.5$ ppt at the node on the computational grid corresponding to the coordinates of the two locations used in this study, the material being uniformly mixed to a depth of 1 m. The model simulation was run until maximum concentration dropped below the 1 ppb level and a concentration profile was generated hourly. Neumann (no flux across boundaries) boundary conditions ($\partial C/\partial x = 0$) were set for boundary planes corresponding to the bottom and all sidewalls except at the boundary corresponding to the inlet of the shipping channel where Dirichlet (fixed concentration) boundary conditions ($C = \text{const.}$) was established.

4. Results

In this section, first we present the results of numerically estimating turbulent diffusivity values. Next, the results of the error analyses performed on the model are presented and finally, results from both model simulation runs. Surface current measurements are represented in Fig. 3 (as a time series at one location within the computational domain) and as current vectors in Fig. 4 (at four successive times over the entire domain). When combined with a linear velocity profile in the vertical coordinate direction, the 3D velocity field necessary for the simulation run was obtained.

The de-tided time series shown by the broken lines in Fig. 3 reveals the tidal variations in velocity. Given the temporal scale of the study (~10 days) tidal variations in current would manifest as turbulent fluctuations about a mean flow velocity, a necessary condition for evaluating diffusivity values in accordance with Eq. (3). The velocity vectors represented in Fig. 4 are color coded and scaled in length to highlight the spatial–temporal variation of current over the computational domain. It is seen from these plots that the current varies in magnitude and direction both in time and space in response to external forcing and turbulent diffusivity is expected to show similar pattern in spatial variation.

4.1. Turbulent diffusivity

The velocity time series used for the eventual computer experiments were obtained over a 10-day period between 17:00 hours on 03/17/2003 and 18:00 hours on 03/27/2003 for each of the coordinate axes on the horizontal plane. Following the application of Eq. (3), the distribution density function for diffusivity was obtained. The density and spatial distribution of diffusivity values are shown in Figs. 5 and 6, respectively. As shown in Fig. 5, the statistical properties of the distribution

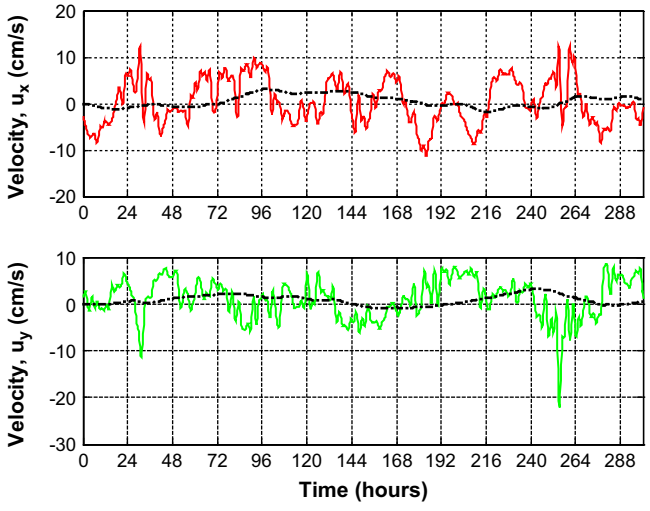

Fig. 3. Typical velocity time series from surface current measurements at one location in the computational grid, shown as a time series (solid line) and the de-tided signal (dotted line) for east–west (top panel) and north–south (lower panel) coordinate axes.

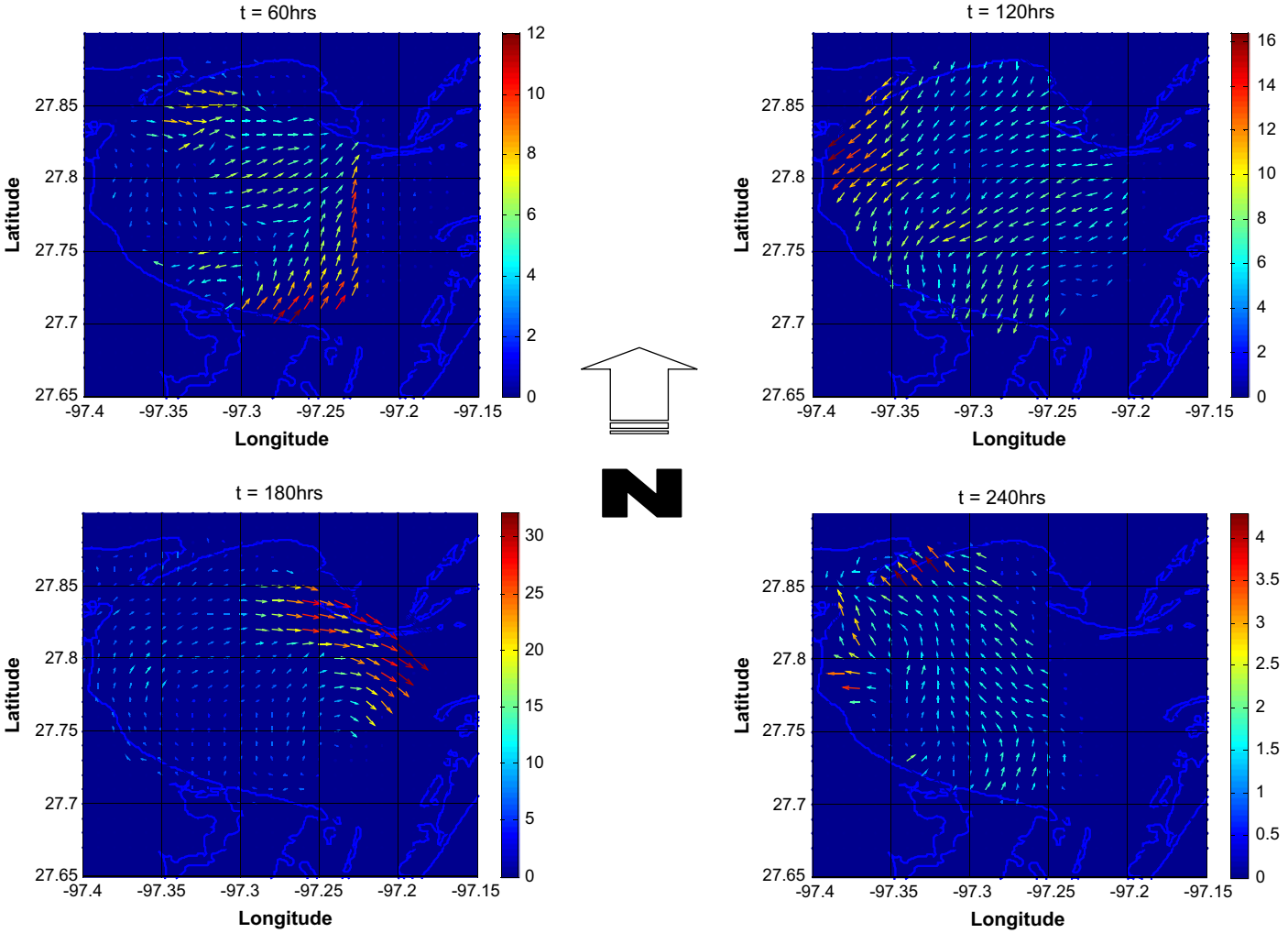

Fig. 4. From top left to bottom right, the spatial distribution of current vector (colored arrows, current measured in cm/s) at time $t = 60$, 120, 180 and 240 h.

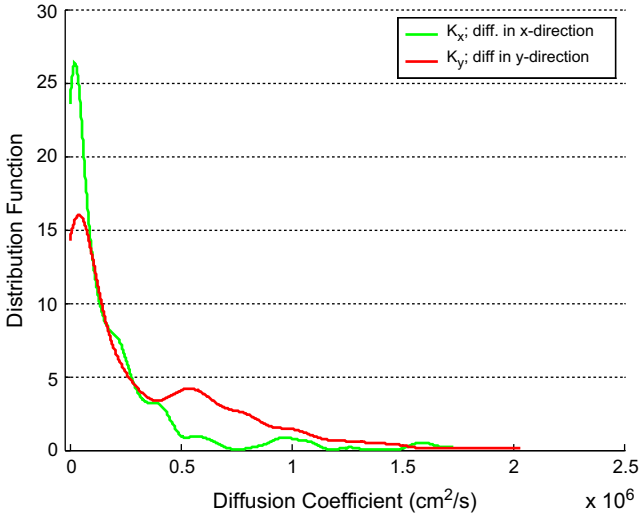

Fig. 5. Distribution density for turbulent diffusivity along the coordinate axes.

exhibit log-normality. This is to be expected since the underlying environmental parameter is constrained by zero minimum, exhibits all non-negative values and high variability with relatively small number of extreme values. The underlying distribution of diffusivity values are seen to fall within the range $K_x = 8.62 \pm 4.98 \times 10^5$ cm^2/s in the x-coordinate direction, and $K_y = 1.01 \pm 0.58 \times 10^6$ cm^2/s in the y-coordinate direction.

From Fig. 6, it is seen that there are localized areas of extreme diffusivity values. The mixing process in these regions is expected to be relatively higher in intensity and would result in a higher rate of growth in size of a diffusing cloud. The implications of this variability with respect to rate of growth captured in spatially distributed turbulent diffusivity or diffusion coefficient will be investigated in the next sub-section.

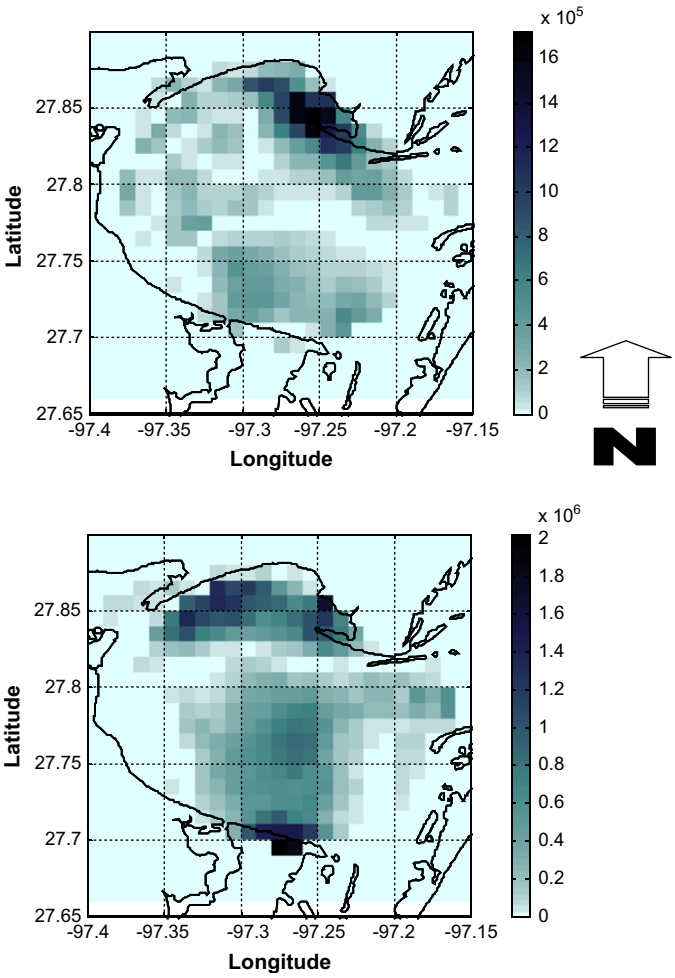

Fig. 6. Spatial distribution of turbulent diffusivity; top panel, diffusivity K_x in x-direction (modal value $= 2.1 \times 10^4$ cm^2/s; bottom panel, diffusivity K_y in y-direction (modal value $= 4.0 \times 10^4$ cm^2/s).

Table 2
Variance and spatial location estimates of a dye patch from an instantaneous point discharge for different values of Re (constant velocities)

	Distance of center of mass relative to origin (m)		Computed variance (m^2)		Cell Reynolds number, Re		Velocity (cm/s)		Diffusion coefficient (cm^2/s)	
	x-coordinate	y-coordinate	x-direction	y-direction	x-dir	y-dir	u	v	K_x	K_y
(A)										
Actual	540	1620	1.08×10^4	1.08×10^5	100	30	10	30	1×10^4	1×10^5
Numeric	273	914	2.78×10^5	9.11×10^5						
Actual	540	1620	1.08×10^5	1.08×10^6	10	3	10	30	1×10^5	1×10^6
Numeric	323	1380	3.25×10^5	1.35×10^6						
Actual	540	1620	1.08×10^6	1.08×10^7	1	0.3	10	30	1×10^6	1×10^7
Numeric	534	1595	1.07×10^6	1.06×10^7						
(B)										
Actual	346	1037	6.91×10^3	6.91×10^4	50	15	10	30	1×10^4	1×10^5
Numeric	180	646	9.23×10^4	3.13×10^5						
Actual	346	1037	6.91×10^4	6.91×10^5	5	1.5	10	30	1×10^5	1×10^6
Numeric	244	1034	1.22×10^5	6.86×10^5						
Actual	346	1037	6.91×10^5	6.91×10^6	0.5	0.15	10	30	1×10^6	1×10^7
Numeric	343	1020	6.85×10^5	6.80×10^6						

(A) Grid Res $= 1000 \times 1000 \times 1$; Number of nodes $= 4056$; Time elapsed $= 3 \times 1800$ s. (B) Grid Res $= 500 \times 500 \times 1$; Number of nodes $= 15\,606$; Time elapsed $= 3 \times 1152$ s (6×900 s).

Table 3
Variance and spatial location estimates of a dye patch from an instantaneous point discharge for different values of *Re* (constant diffusivities)

	Distance of center of mass relative to origin (m)		Computed variance (m^2)		Cell Reynolds number, *Re*		Velocity (cm/s)		Diffusion coefficient (cm^2/s)	
	x-coordinate	*y*-coordinate	*x*-direction	*y*-direction	*x*-dir	*y*-dir	*u*	*v*	K_x	K_y
(A)										
Actual	360	1080	7.20×10^5	7.20×10^6	1.0	0.3	10	30	1×10^6	1×10^7
Numeric	316	966	6.30×10^5	6.44×10^6						
Actual	720	2160	7.20×10^5	7.20×10^6	2.0	0.6	20	60	1×10^6	1×10^7
Numeric	558	1863	1.53×10^6	7.14×10^6						
Actual	1080	3240	7.20×10^5	7.20×10^6	3.0	0.9	30	90	1×10^6	1×10^7
Numeric	799	2887	7.86×10^5	6.22×10^6						
(B)										
Actual	360	1080	7.20×10^5	7.20×10^6	0.5	0.15	10	30	1×10^6	1×10^7
Numeric	318	963	6.33×10^5	6.40×10^6						
Actual	720	2160	7.20×10^5	7.20×10^6	1.0	0.3	20	60	1×10^6	1×10^7
Numeric	633	1926	6.25×10^5	6.32×10^6						
Actual	1080	3240	7.20×10^5	7.20×10^6	1.5	0.45	30	90	1×10^6	1×10^7
Numeric	953	2893	6.18×10^5	6.19×10^6						

(A) Grid Res = 1000 × 1000 × 1; Number of nodes = 15 606; Time elapsed = 4 × 900 = 3600 s. (B) Grid Res = 500 × 500 × 1; Number of nodes = 15 606; Time elapsed = 4 × 900 = 3600 s.

4.2. Error analyses

Tables 2–4 present the error estimates comparing between the analytical and numerical solutions with varying *Re* values. In Table 2, the advective coefficients were held constant while varying the diffusivities. In Table 3, the advective coefficients were varied while holding constant, the diffusivities. Estimates made of the variance of the diffusing cloud and the location of its center of mass were computed for both the analytical and numerical solutions. Model error representing the difference between these two computations were determined as summarized in Table 4 and presented graphically in Figs. 7 and 8.

Comparing the model error for center of mass (Fig. 7) and variance (Fig. 8) estimates of the patch indicates that the error in the spread of the diffusing patch resulting from a release of material at the injection location increases with increasing *Re* (the largest errors occurring at $Re > 2$). This is associated with changing diffusivity values (velocity being held constant), going up to as much as a 25-fold difference in variance estimates at $Re = 100$. Very little effect on variance estimates due to changing velocity values can be observed even at $Re > 2$. Noting that estimates of diffusivities can be off by orders of magnitude if one does not account for the spatial distribution of diffusivity, it becomes apparent from these results that errors in diffusivity values make the numerical scheme more error prone in predicting the size of a diffusing patch. It is also apparent from comparing Figs. 7 and 8 that the model tends to overestimates the spatial location of the patch while it tends to underestimate the spread (or size of the patch) with increasing *Re*. Therefore, size predictions are more significantly affected from using inaccurate diffusivity estimates, less so directly from using inaccurate current measurements.

Table 4
Normalized error from numerical estimates of variance and spatial location in comparison with exact solution for different values of *Re*

Normalized error; variable dispersion, constant velocities			Normalized error; constant dispersion, variable velocities		
Cell Reynolds number, *Re*	Error		Cell Reynolds number, *Re*	Error	
	Variance estimates	Spatial location		Variance estimates	Spatial location
100	−24.7	0.49	1	0.13	0.12
10	−2.01	0.40	2	−1.13	0.23
1	9.26×10^{-3}	1.11×10^{-2}	3	-9.17×10^{-2}	0.26
50	−12.4	0.48×10^{-1}	0.3	0.12	0.12
5	−0.77	2.95×10^{-1}	0.6	0.13	0.12
0.5	8.68×10^{-3}	8.67×10^{-3}	0.9	0.14	0.12
30	−7.44	4.36×10^{-1}	0.5	0.11	0.11
3	−0.25	1.48×10^{-1}	1.0	8.33×10^{-3}	0.14
0.3	1.85×10^{-2}	1.54×10^{-2}	1.5	0.14	0.11
15	−3.53	0.38	0.15	0.11	0.11
0.5	7.24×10^{-3}	2.89×10^{-3}	0.3	0.12	0.11
0.15	1.59×10^{-2}	1.64×10^{-2}	0.45	0.14	0.11

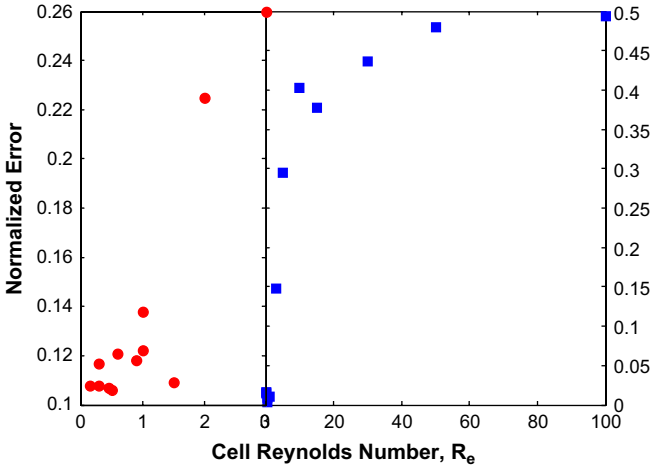

Fig. 7. Normalized error from model simulation runs for spatial location of plume with varying *Re*; -●-, constant diffusivity, varying velocity; -■-, varying diffusivity, constant velocity.

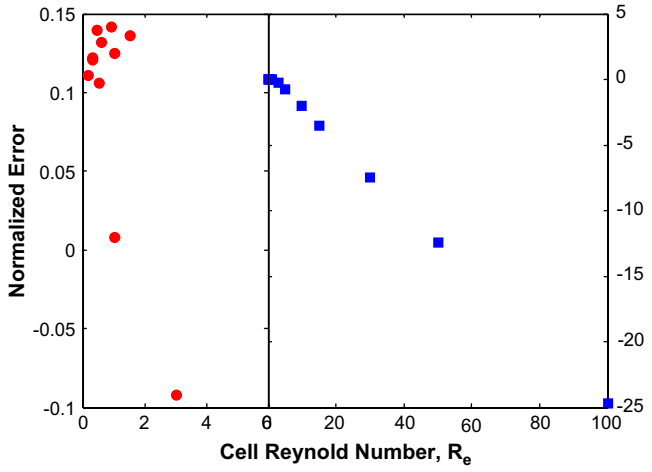

Fig. 8. Normalized error from model simulation runs for variance of concentration distribution with varying *Re*; -●-, constant diffusivity, varying velocity; -■-, varying diffusivity, constant velocity.

Finally, given the distribution of diffusivity values as shown in Fig. 5 and the target diffusivity values for model error analysis ($K_x = 1 \times 10^4 - 10^5$ cm^2/s and $K_y = 1 \times 10^5 - 10^6$ cm^2/s), the model was run for comparison with the analytical solution using values within the specified target range for diffusivity. The base grid for the computational domain was $1000 \times 1000 \times 1$ m and the computational time-step was set at 1 s. The resulting concentration profiles are shown in Fig. 9 in comparison with the analytical form. The agreement between the numerical results and the exact solution is quite good indicating that the model does not appear to introduce any significant amount of numerical dissipation and dispersion.

4.3. Model simulation run

Results from the two example injection locations indicate the differences, particularly in the variance estimates obtained

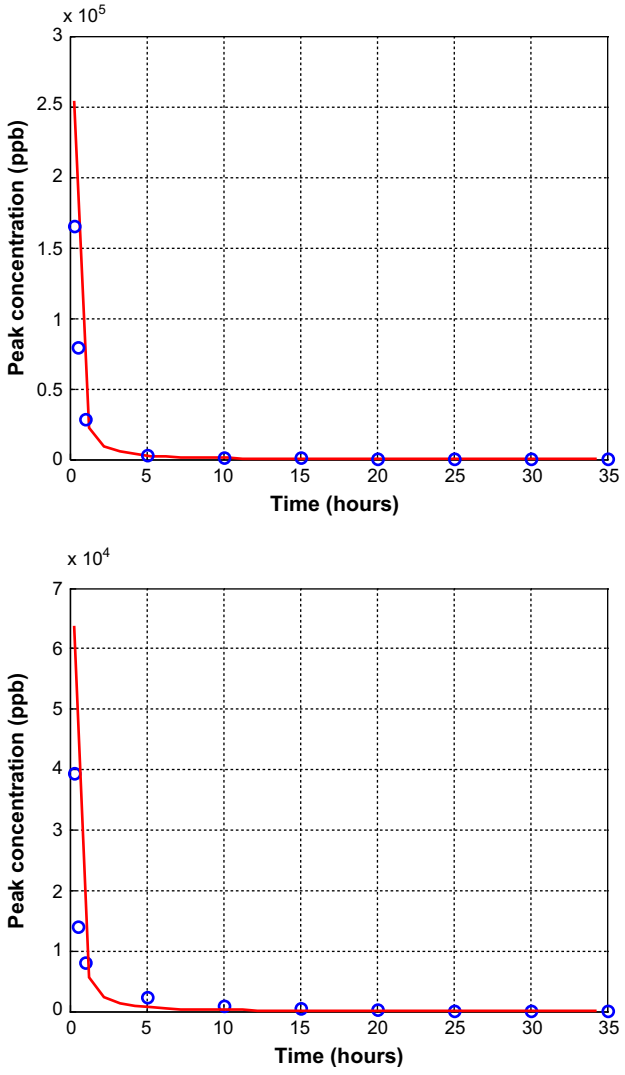

Fig. 9. Plot of peak concentration against time; top panel, $K_x = 1 \times 10^4$, $K_y = 1 \times 10^5$; bottom panel, $K_x = 1 \times 10^5$, $K_y = 1 \times 10^6$. Solid line, exact solution, open circle, results from model simulation.

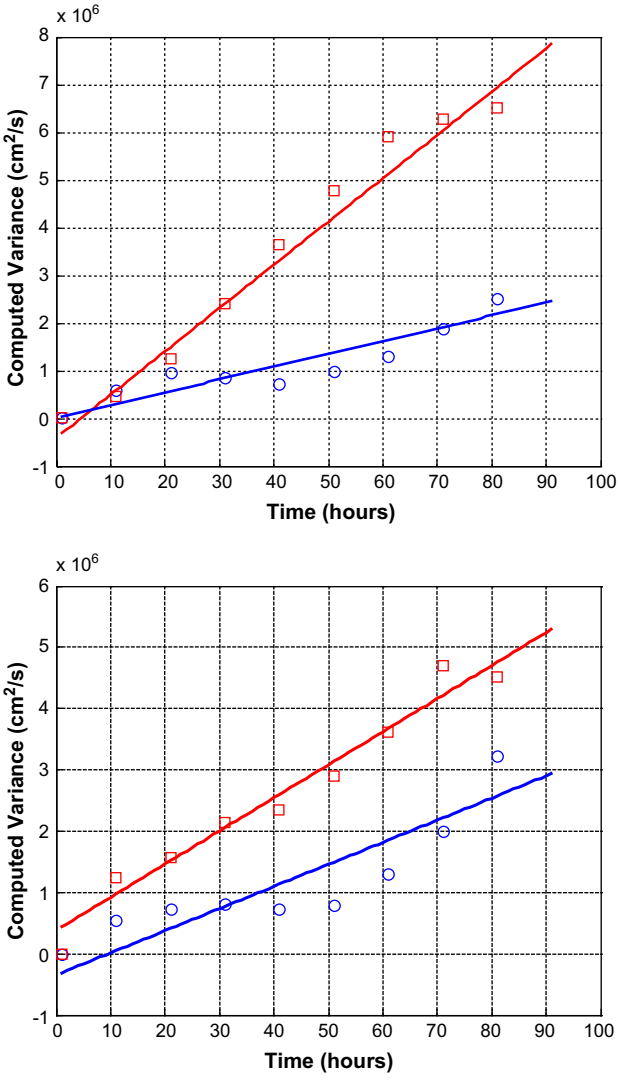

Fig. 10. Plot of variance of concentration for pulse discharge initialized at two different locations within the computational domain. The difference in variance attributable to the difference in diffusivity values dependent on spatial location.

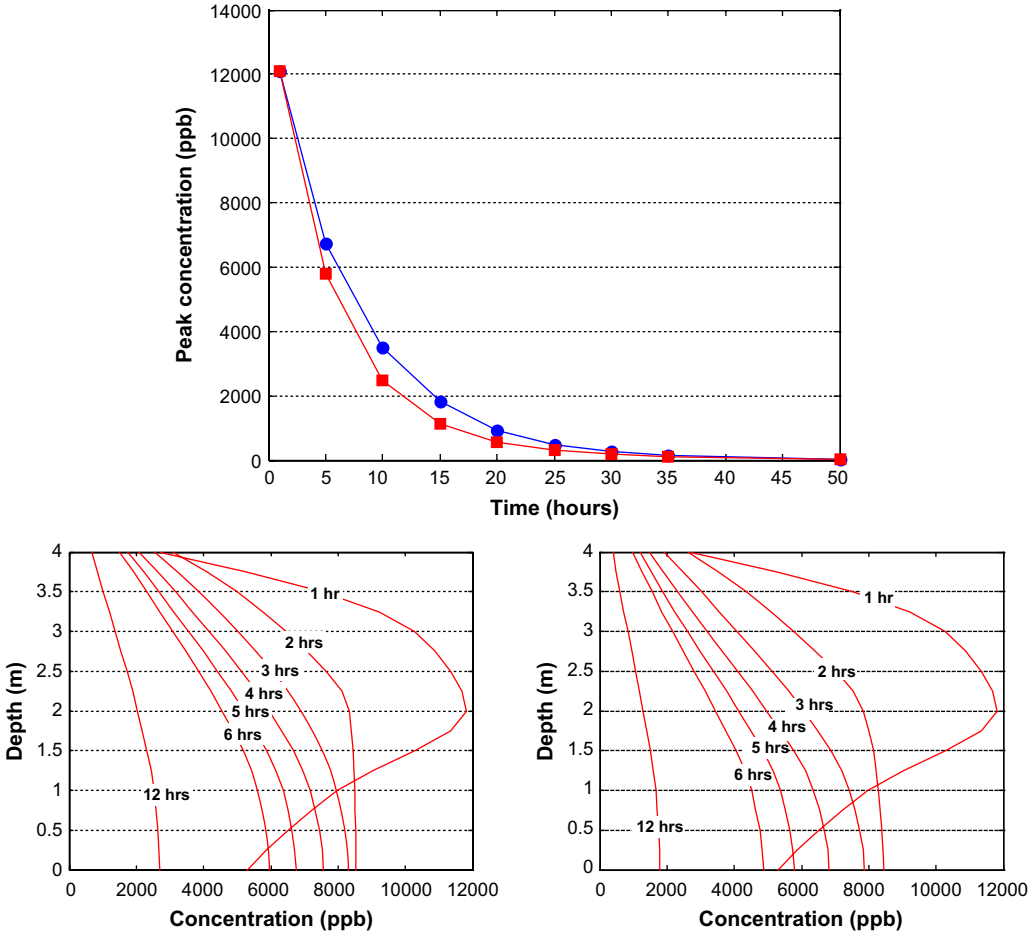

Fig. 11. Top panel; peak concentration vs. time for scenario 1 (-●-) and scenario 2 (-■-). Bottom left panel; vertical profile from run #1. Bottom right panel; vertical profile from run #2.

after 90 h of tracking an instantaneous pulse discharge. The difference in variance of the concentration profile along each of the coordinate axis can be seen in Fig. 10, the slope of the variance–time plots being remarkably different. More importantly, and a direct consequence of the differences in diffusivities with respect to location, was the observed slope of the variance–time plot being considerably steeper particularly along the *y*-coordinate direction in the first model run compared to the second. This observation is underscored by the concentration profiles displayed in Fig. 11, a plot of peak concentration vs. time. The difference in peak values particularly between 5 and 25 h following the introduction of the conservative, neutrally buoyant material into the body of water can be observed. Therefore, we observe differences in both spatial extent as well as peak concentration values of the diffusing material, differences that can be readily attributed to the spatial variation in observed diffusivities, which implies that the mixing process was stronger in some parts of the bay compared to others.

In addition, the diffusing material would be seen to grow at a faster rate in one scenario compared to the other, the computed variance in the *y*-coordinate direction being remarkably different between the two scenarios modeled. In both scenarios, the growth along the *y*-coordinate direction was higher than the growth along the *x*-coordinate direction. This observation would not have manifested had the simulation employed spatially uniform diffusivities, which would be the case if diffusivity values were obtained using diffusion diagrams or if they were based in results from tracer experiments. Whereas a number of turbulence closure schemes exist, which might capture the dynamics of the water body in terms of the mixing coefficients, these schemes are difficult to implement and lack sufficient data to support their applicability. By contrast, the scheme presented here is relatively simple and has been validated with data from a related study combining current measurements with data from the evolution of a dye patch (Ojo et al., submitted for publication-a-b, in press).

Tables 5 and 6 summarize the results displayed in Figs. 10 and 11. Concentration profiles of the material at six successive times for each of the two scenarios are displayed in Figs. 12 and 13 showing the evolution of the material with time with the currents overlayed. From the vertical profiles of the peak concentration presented in Fig. 11, it can be observed that in this shallow body of water the conservative neutrally buoyant constituent becomes fully mixed into the water column about 12 h following release. It is instructive to note that the profile is similar to what one would obtain from an elevated source release in atmospheric applications.

Table 5
Peak concentration at successive time intervals for modeled scenarios

Time elapsed (h)	Peak concentration (ppb)	
	Scenario 1	Scenario 2
1	12 100	12 100
5	6750	5780
10	3510	2470
15	1820	1110
20	926	537
25	468	295
30	273	167
35	162	96
50	29	19

Some general comments about the behavior of the patch are given here. In both runs, the release occurred towards the end of the ebb tide and about the beginning of flood. The patch would be observed to orient itself in an east–west direction after a few hours into the run and at approximately 24 h following release, begins to orient itself in a north–south direction eventually becoming elongated in this direction. The patch did not exit the computational domain during both runs but during run #1, it makes contact at the southernmost edge with land after approximately 48 h while it begins to move towards the Laguna Madre located on the eastern boundary. In run #2, contact was made with land on the northernmost tip of the patch after approximately 60 h, while moving towards the shipping channel entrance. In both runs, the constituent impacts the bottom long before it makes contact with any land boundaries and in this shallow bay, this may be the most important consideration especially if one were interested in the effect of a pollutant on the benthos. This of course would be influenced by other factors including the properties of the constituent of interest and its interactions with other constituents within the water column.

5. Conclusion

The modeling framework presented here addresses the hydrodynamic data requirements and parameterization of a transport model for constituent tracking in surface waters. The result was a simplified CTM that provided improved accuracy for predicting concentration profiles of constituents of interest and would allow for better tracking of plumes in surface waters. Within this modeling framework, calibration would be performed once on the algorithm for evaluating turbulent diffusivity and the implication for modelers, emergency responders as well as decision makers is a near real-time contaminant transport and monitoring system that can be deployed rapidly in any body of water where surface current mapping can be applied.

Table 6
Variance-time summary for modeled scenarios

Elapsed time (h)	Scenario 1		Scenario 2	
	Variance in x-direction ($cm^2/s \times 10^6$)	Variance in y-direction ($cm^2/s \times 10^6$)	Variance in x-direction ($cm^2/s \times 10^6$)	Variance in y-direction ($cm^2/s \times 10^6$)
1	–	–	–	–
10	0.56	0.43	0.50	1.17
20	0.94	1.18	0.69	1.53
30	0.90	2.23	0.79	2.21
40	0.68	3.53	0.74	2.28
50	0.95	4.78	0.77	2.90
60	1.25	5.76	1.27	3.68
70	1.84	6.25	1.87	4.80
80	2.43	6.58	3.09	4.43
90	3.03	6.94	4.00	5.37

In this study, we: (1) Developed a numerical scheme for evaluating turbulent diffusivity from hydrodynamic observations; (2) Decoupled hydrodynamic computations from the overall transport modeling framework by incorporating direct observations of velocity into a CTM; (3) Evaluated model performance against analytical solutions of the governing transport equations, capturing the dynamics of transport and mixing process inherent in both advection and turbulent diffusion; (4) Developed a simplified model for 3D constituent transport and plume trajectory tracking driven by direct hydrodynamic observations using surface current measurements from HF Radar.

Spatially distributed diffusivities were computed from the temporal fluctuations of velocity and applied within the model framework. Traditionally the diffusivities, K_x, K_y, K_z would be taken to be constant over the domain of interest, and these coefficients being determined from tracer experiments or taken from diffusion diagrams may not adequately account for the anisotropic characteristic within the domain of interest. Although coupled models employing DNS and turbulence closure schemes may capture this property of a turbulent flow field, they are difficult to implement and deploy within the context of emergency response. In this study, the advective flux coefficients (u_x, u_y, u_z) were obtained directly from radar while the diffusive flux coefficients (K_x, K_y, K_z) were obtained through the resulting velocity time series.

Through a series of computer experiments we were able to show that by taking into account the heterogeneous nature of the turbulent field in surface waters such as bays and estuaries, better accuracy would be achieved in model predictions. The accuracy of the data-driven CTM was tested against analytical solutions and two instantaneous releases of conservative material were successfully modeled using this simplified model. As seen from the results, model error in terms of peak concentration and spatial location may not be quite as significant (Figs. 7–11) relative to the error in terms of spatial extent. The ramification from a response perspective is that the worst performing model might be able to locate a diffusing patch but be considerably impacted in its ability to determine where or when it makes landfall.

In the light of the allocation of resources for countermeasures viz. Emergency Response and Homeland Security, an operational real-time environmental and oceanographic assessments system in surface waters provides a very valuable tool and it becomes very important to be able to reduce uncertainties inherent in the parameterization of the associated numerical models. The

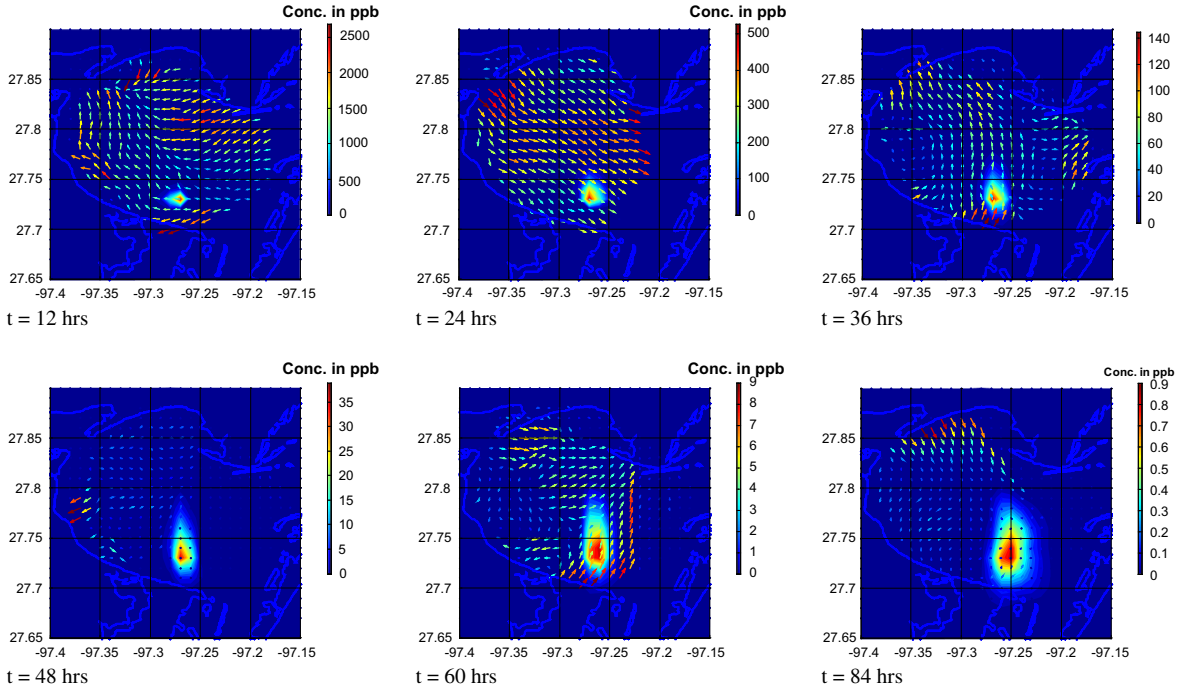

Fig. 12. Evolution of diffusing conservative material over three tidal cycles; run #1. The arrows representing the current vectors are colored for relative strength from blue to red on a scale of 0–150 cm/s.

data-driven scheme developed here for Corpus Christi Bay, TX would afford us this capability. The model developed is simple to deploy and easy to configure and would be very useful for emergency response activities as it takes actual hydrodynamic observations as input thereby capturing the variability that is characteristic of shallow wind-driven bays.

5.1. Future work

In terms of the current mapping created by HF Radar, there remains work to be done in ensuring that gaps are removed from the data set particularly with respect to spatial coverage. One way of doing this is to develop data assimilation

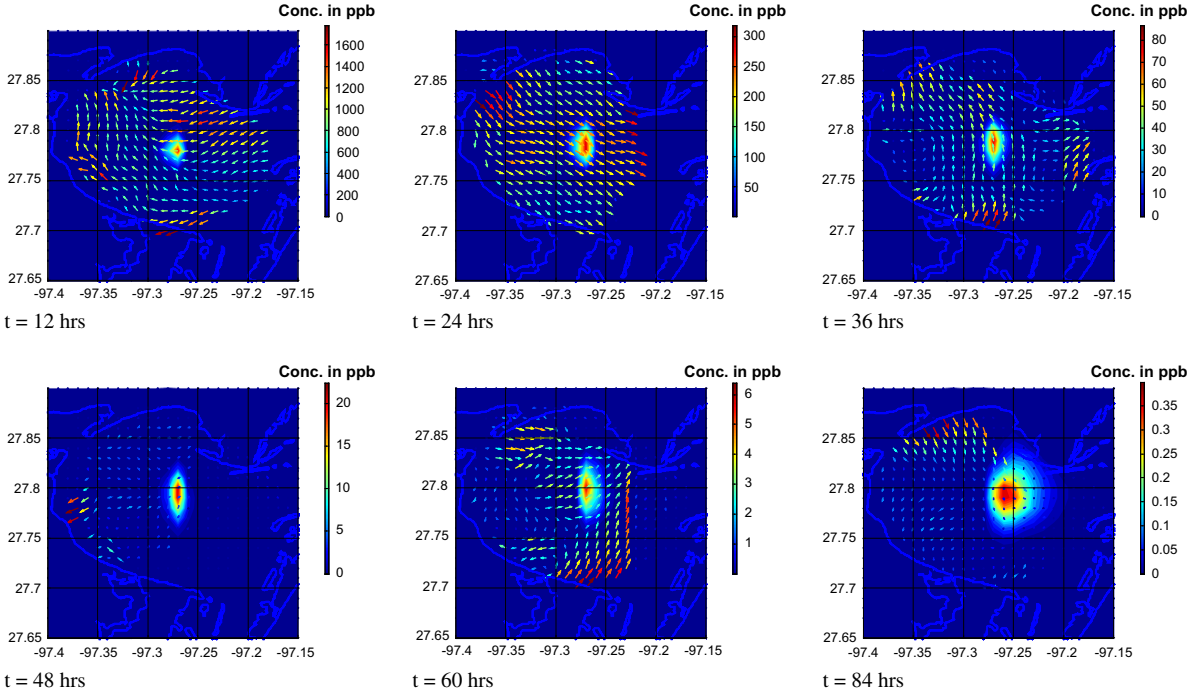

Fig. 13. Evolution of diffusing conservative material over three tidal cycles; run #2. The arrows representing the current vectors are colored for relative strength from blue to red on a scale of 0–150 cm/s.

techniques or spatial interpolation techniques that would allow for a better representation of the surface currents during those times that the data set from radar may suffer degradation. In this study, simple spatial interpolation methods were used and may not be robust enough but would suffice within this conceptual framework. An operational model will need to consider these limitations in addition to the need to couple bio-geochemical interactions, which is the subject of ongoing research within our laboratory.

Acknowledgement

This work was funded in part by funds from Texas Higher Education Coordinating Board (THECB-TDT 011161-0011-2001) and by funds from National Science Foundation (NSR-MRI C02-00533). Special thanks go to the Texas General Land Office (TGLO) in providing support for this project. The authors would also like to thank the research staff at the Shoreline Environmental Research Facility at Texas A&M University for helping with the data collection.

References

Barrick, D.E., Headrick, J.M., Bogle, R.W., Crombie, D.D., 1977. Ocean surface currents mapped by radar. Science 198, 138–144; Batchelor, G.K., 1953. Homogeneous Turbulence. Cambridge University Press, Cambridge, UK, 197 pp.

Blom, J.G., Verwer, J.G., 1996. Algorithm 759: VLUGR3: a vectorizable adaptive-grid solver for PDEs in 3D – Part II. Code description. ACM Transactions on Mathematical Software 22, 329–347.

Bowden, K.F., Howe, M.R., 1963. Observations of turbulence in a tidal current. Journal of Fluid Mechanics 17, 271–284.

Csanady, G.T., 1980. Turbulent Diffusion in the Environment. D. Reidel Publishing Co., Holland/Boston, USA; London, England, 248 pp., reprinted.

Elder, J.W., 1958. The dispersion of marked fluid in turbulent shear flow. Journal of Fluid Mechanics 8, 33–40.

Elliot, A.J., 1986. Shear diffusion and the spread of oil in the surface layers of the North Sea. Deutshe hydrographische Zeitschrift 39, 114–137.

Ernest, A.N., Bonner, J.S., Autenrieth, R.L., 1991. Model parameter-estimation for particle-transport. Journal of Environmental Engineering–ASCE 117, 573–594.

Fletcher, C.A.J. (Ed.), 1991. Computational Techniques for Fluid Dynamics: Springer Series in Computational Physics, vol. 1. Springer.

Kelly, F.J., Bonner, J.S., Ojo, T.O., Durel, A., 2004. Port Freeport's "FlowInfo": an example of an Integrated Port Navigation and Environmental Data System (IPNEDS). In: ASCE Ports 2004 Conference.

Lam, D.C., Murthy, C.R., Simpson, R.B., 1983. Effluent Transport and Diffusion Models for the Coastal Zone. Springer-Verlag.

Lee, D.G., Bonner, J.S., Garton, L.S., Ernest, A.N., Autenrieth, R.L., 2000. Modeling coagulation kinetics incorporating fractal theories: a fractal rectilinear approach. Water Research 37, 1987–2000.

Lehr, W., Robert, J., Evans, Mary, Simecek-Beatty, Debra, Overstreet, Roy, 2002. Revisions of the ADIOS oil spill model. Environmental Modelling & Software 17, 191–199.

List, J., Gartrell, G., Winant, C., 1990. Diffusion and dispersion in coastal waters. Journal of Hydraulic Engineering 116, 1158–1179.

Martin, J.L., McCutcheon, S.C., 1998. Hydrodynamics and Transport for Water Quality Modeling. CRC Press, Boca Raton, FL, 810 pp.

Murthy, C.R., 1975. Horizontal diffusion characteristics in Lake Ontario. Journal of Geophysical Research 6, 76–84.

McCay, D.F., 2003. Development and application of damage assessment modeling: example assessment for the North Cape oil spill. Marine Pollution Bulletin 47, 341–359.

O'Connor, T.P., Walker, H.A., Paul, J.F., Bierman, Victor J., 1985. A strategy for monitoring of contaminant distributions resulting from proposed sewage sludge disposal at the 106-mile ocean disposal site. Marine Environmental Research 16, 127–150.

Ojo, T., Bonner, J., 2002. 3-Dimensional self-calibrating coastal oil spill trajectory tracking and contaminant transport using HF Radar. In: Proceedings of the Twenty-Fifth Arctic and Marine Oilspill Progam (AMOP) Technical Seminar, pp. 215–226.

Ojo, T.O., Bonner, J.S., Page, C.A. Diffusion and mixing experiments in Corpus Christi Bay, TX: dye-tracer study to determine diffusivity values. Estuarine, Coastal and Shelf Science, submitted for publication-a.

Ojo, T.O., Bonner, J.S., Page, C.A. Observations of shear-augmented diffusion processes and evaluation of effective diffusivity from current measurements in Corpus Christi Bay. Continental Shelf Research, in press.

Ojo, T.O., Bonner, J.S., Page, C.A. Studies on turbulent diffusion processes and evaluation of diffusivity values from hydrodynamic observations in Corpus Christi Bay. Continental Shelf Research, submitted for publication-b.

Ojo, T.O., Bonner, J.S., Sterling, M.C., Fuller, C.B., Page, C.A., Autenrieth, R.L., 2003. Implementation of Distributed Computing System for Emergency Response and Contaminant Spill Monitoring In: Twenty-sixth Arctic and Marine Oilspill Program (AMOP) Technical Seminar, pp. 287–297.

Okubo, A., 1971. Oceanic diffusion diagrams. Deep-Sea Research 18, 789–802.

Application of a hazard-assessment research strategy for waste disposal at 106-mile ocean disposal site. In: Paul, J.F., Victor, J., Bierman, J., Walker, H.A., Gentle, J.H. (Eds.), Oceanic Processes In Marine Pollution, vol. 4. Robert E. Krieger Publishing Company, Malabar, Florida, 286 pp.

Reed, M., Daling, P., Lewis, A., Ditlevsen, M.K., Brørs, B., Clark, J., Aurand, D., 2004. Modelling of dispersant application to oil spills in shallow coastal waters. Environmental Modelling & Software 19, 681–690.

Ruan, F., McLaughlin, D., Li, S., 1999. A general technique for assessing the numerical accuracy of solute transport models. Water Resources Research 35, 3961–3966.

Spaulding, M.L., Mendelsohn, D.L., Swanson, J.C., 1999. WQMAP: an integrated three-dimensional hydrodynamic and water quality model system for estuarine and coastal applications. Marine Technology Society Journal 33, 38–54.

Sterling, J., Michael, C., Bonner, J.S., Ernest, A.N.S., Page, C.A., Autenrieth, R.L., 2004a. Characterizing aquatic sediment-oil aggregates using in situ instruments. Marine Pollution Bulletin 48, 533–542.

Sterling Jr., M.C., Bonner, J.S., Page, C.A., Fuller, C.B., Ernest, A.N., Autenrieth, R.L., 2004b. Modeling crude oil droplet-sediment aggregation in nearshore waters. Environmental Science and Technology 38, 4627–4634.

Taylor, G.I., 1920. Diffusion by continuous movements. Proceedings of the London Mathematical Society 20, 196–211.

Taylor, G.I., 1953. Dispersion of soluble matter in solvent flowing slowly through a tube. Proceedings of the Royal Society of London Series A 219, 186–203.

Taylor, G.I., 1954. The dispersion of matter in Turbulent flow through a pipe. Proceedings of the Royal Society of London Series A 446–467.

Wijesekera, H.W., Allen, J.S., Newberger, P.A., 2003. Modeling study of turbulent mixing over the continental shelf: Comparison of turbulent closure schemes. Journal of Geophysical Research (Oceans) 108 (C3), 3103.